ADVANCED MATERIALS TECHNOLOGIES
www.advmattechnol.de

Roll-to-Roll (R2R) Production of Large-Area High-Performance Piezoelectric Films Based on Vertically Aligned Nanocolumn Forests

*Armen Yildirim, Jesse C. Grant, Siamak Shams Es-haghi, Wojae Lee, Murali Kannan Maruthamuthu, Mohit Verma, John W. Sutherland, and Mukerrem Cakmak**

The recent advances in flexible piezoelectric technologies have sparked a great interest in developing multifunctional next-generation transducers, which are in high demand for various challenging applications. Here, novel quasi 1–3 piezoelectric films with record-high piezoelectric voltage coefficients (g_{33}), reaching up to 0.709 Vm N^{-1}, ≈20% greater than the recently reported highest g_{33} value in the literature, are reported. These composites are constructed via dielectrophoretic alignment of lead zirconate titanate (PZT) particles enhanced by graphene nanoplatelets, leading to densely structured cone-shaped nanocolumn forests in the thickness direction. To demonstrate its potential applications, both structured and randomly dispersed samples are characterized and used in various applications ranging from energy harvesting to structural and personal health monitoring. Furthermore, when placed on the sensor surface, the oriented piezoelectric films are shown to detect even the slight movements of a small-sized insect, demonstrating the ultrasensitivity of the system. Finally, to show the scalability of the dielectrophoretic process, a large area sample (12 ft long and 6-in.-wide) is also produced continuously via a novel multifunctional custom designed roll-to-roll manufacturing line. To the best of the knowledge, this is the largest single piece of piezoelectric film ever reported in the literature.

Dr. A. Yildirim, J. C. Grant, Dr. S. Shams Es-haghi, Prof. M. Cakmak
School of Materials Engineering
Birck Nanotechnology Center
Purdue University
West Lafayette, IN 47907, USA
E-mail: cakmak@purdue.edu

W. Lee
Environmental and Ecological Engineering
Purdue University
West Lafayette, IN 47907, USA

Dr. M. K. Maruthamuthu, Prof. M. Verma
Department of Agricultural and Biological Engineering
Birck Nanotechnology Center
Purdue University
West Lafayette, IN 47907, USA

Prof. J. W. Sutherland, Prof. M. Cakmak
School of Mechanical Engineering
Purdue University
West Lafayette, IN 47907, USA

The ORCID identification number(s) for the author(s) of this article can be found under https://doi.org/10.1002/admt.202000553.

DOI: 10.1002/admt.202000553

1. Introduction

Piezoelectricity plays a major role in many modern-day applications, ranging from underwater ultrasonic transducers[1,2] to accelerometers in space shuttles.[3–5] In general, today's state-of-the-art piezoelectric materials and devices depend heavily on ceramics due to their outstanding electromechanical coupling properties, but some disadvantages still remain, such as the lack of mechanical flexibility and the ability to tune properties for a specific use. To address these challenges, polymer-based piezoelectric nanocomposites (PNCs) have emerged as a potential alternative to their ceramic counterparts. PNCs not only provide outstanding piezoelectric coefficients, but also exhibit tailorable mechanical properties and ease of processability, which makes them promising candidates for applications where flexibility and tunability are essential.[6–13] In addition, PNCs can also play a pivotal role in the development of self-powered micro- and nanoscale devices by harvesting wasted kinetic energy from already existing and ubiquitous ambient sources[9] such as structural vibrations from industrial machinery[14,15] (e.g., vehicles, motors, etc.), everyday human activities[16–20] (e.g., walking, running, breathing, etc.), and inexhaustible natural energy resources[21] (e.g., water waves, wind, etc.).

According to the systematic framework introduced by Newnham et al.,[22] two-phase (diphasic) piezoelectric composites can be categorized through the connectivity of each constituent phase. Among ten different connectivity patterns, 1–3 piezocomposites have attracted a great deal of attention and have been widely used in numerous applications[7,23–25] due to their unique electromechanical properties, especially when the filler is aligned in the "Z" (thickness) direction. In these composites, the piezoelectric phase (e.g., particle, fiber, rod, or nanowire) is aligned and connected in one dimension (x, y, or z), whereas the polymer phase is continuous in all three dimensions. One of the strategies to achieve high-performance 1–3 composites is via electric-field assisted alignment of

piezoelectric phase.[8,26–33] This technique is based on the dielectrophoresis (DEP) principle and can significantly improve the piezoelectric properties of composites even at low filler concentrations due to the formation of high aspect-ratio columns, also known as pearl-chains, in a particular dimension. For instance, alignment of lead zirconate titanate nanowires (PZT NWs) in a polyvinylidene fluoride (PVDF) matrix has been proven to enhance the energy density of the nanocomposite up to 51.6% compared with randomly oriented NWs.[34] Likewise, an 88% increase in voltage output was reported when the PZT NWs were aligned in a polydimethylsiloxane (PDMS) matrix.[30] Recently, Gao et al. also reported an ultrahigh piezoelectric voltage constant (g_{33}) of 600×10^{-3} V m N^{-1} with dielectrophoretically aligned $(Ba_{0.85}Ca_{0.15})(Ti_{0.90}\,Zr_{0.10})O_3$ (BCZT) particles.[33]

DEP phenomenon is based on the polarization of particles in a nonuniform electric field and the force (F_{DEP}), which acts on the induced dipole moment of a particle and creates a translational motion, is along the direction of the field gradient (∇E). The force F_{DEP} is given by Equation (1)[35]

$$F_{DEP} = 2\pi R^3 \varepsilon_0\, \varepsilon_m\, [CM] \nabla E^2 \tag{1}$$

where R is the radius of the particle, ε_0 is the permittivity of vacuum (8.85×10^{-12} F m^{-1}), and the ε_m is the relative dielectric constant of the matrix, and [CM] is the Clausius–Mossotti factor. The factor [CM], given in Equation (2),[36] is determined by the dielectric properties of the particle and the surrounding matrix

$$[CM] = \frac{\varepsilon_P - \varepsilon_m}{\varepsilon_P + 2\varepsilon_m} \tag{2}$$

where ε_p is the permittivity of the particle. Thus, Equation (2) implies that the frequency of the applied electric field also plays a vital role during the dielectrophoresis process, since the permittivity of a material is frequency dependent.

Herein, we report the production of novel quasi 1–3 multifunctional piezoelectric films with outstanding piezoelectric voltage coefficients that are based on dielectrophoretic alignment of PZT and graphene nanoplatelets (GNPs) in a PDMS matrix. Furthermore, this process was also proven to be fully compatible with a roll-to-roll based large-scale manufacturing technique, enabling the continuous production of the proposed high-performance piezoelectric composites.

2. Results and Discussion

2.1. Electric-Field Induced Alignment of PZT Particles

In the first part of this work, a systematic investigation was carried out to understand the effect of electric-field strength (E) and frequency (υ) parameters on the alignment of PZT particles in a thermocurable PDMS matrix. The results obtained in this section were then used to select an optimum υ and E value to align different concentrations of PZT. First, a small volume fraction (0.5 vol%) of PZT particles (with bulk d_{33} = 670 pC N^{-1}) was uniformly dispersed in a PDMS resin via a THINKY planetary centrifugal mixer. Subsequently, the curing agent (hardener) was introduced with a base-to-agent ratio of 10:1. As illustrated in **Figure 1**a,b, the PZT/PDMS mixture was then cast between two parallel copper electrodes, which were placed on a glass slide with a 2 mm separation in between. Afterward, the electric-field induced alignment of the PZT particles was investigated at three different frequencies (100 Hz, 1 kHz, and 10 kHz) and at two different field strengths (500 and 1000 V mm^{-1}). To characterize the effect of these parameters on chain-length evolution, for each experiment, the optical microscopy images were taken at various stages: i) before electric-field application, ii) after 5 min, iii) 15 min, and iv) 30 min. These images were then analyzed by ImageJ software and the obtained particle/chain length distributions were described by Burr distribution function given by

$$f(x) = \frac{\frac{\alpha k}{\beta}\left(\frac{x-\gamma}{\beta}\right)^{\alpha-1}}{\left(1+\left(\frac{x-\gamma}{\beta}\right)^{\alpha}\right)^{k+1}} \tag{3}$$

where α, k, β, and γ are the fitting parameters.

Figure 1c,d shows the probability distribution functions of particles/chains at different time intervals for both 500 and 1000 V mm^{-1}, respectively (10 kHz). The corresponding fitting parameters are provided in Tables S1 and S2 of the Supporting Information. The validity of the Burr distribution function to describe the data was verified via Kolmogorov–Smirnov test.[37]

As Figure 1c,d demonstrates, the probability of finding longer chains in a certain time period increases with increasing exposure time. At this stage, in order to perform an effective quantitative comparison between the six different experimental conditions (i.e., two different field strengths and three different frequencies), the mean values of the distributions were calculated and plotted as a function of time (Figure 1e). It is also noteworthy that, before electric-field application, the mean values of each distribution are approximately the same in all conditions (this is important in order to have a valid comparison across all measurements). Upon application of electric field, the mean particle/chain length grows relatively fast in the case of 1000 V mm^{-1} field strength as compared with that of 500 V mm^{-1}. As shown in Equation (1), this result along with the optical images shown in Figure 1e (captured after 30 min of electric-field exposure) supports the quadratic relationship between the dielectrophoretic force (F_{DEP}) and the electric-field gradient (∇E), verifying the importance of electric field on pearl chain formation. Moreover, Figure 1e also displays the effect of frequency on particle alignment, where the highest mean values at 1000 V mm^{-1} were observed at 100 Hz and exhibited a decreasing trend with increased frequency. This can be presumably attributed to the fact that at high voltage and a relatively high frequency, the PZT particles are no longer able to reorient their dipoles fast enough with the alternating field and therefore cannot create as strong dipoles as in the case of lower-frequency values. Based on these results, 1000 V mm^{-1} and 100 Hz were selected for the alignment of PZT particles in a silicone based PDMS resin.

During the dielectrophoretic alignment, the optical transparency of the system also increases in the electric-field direction due to the formed particle-depleted zones between neighboring

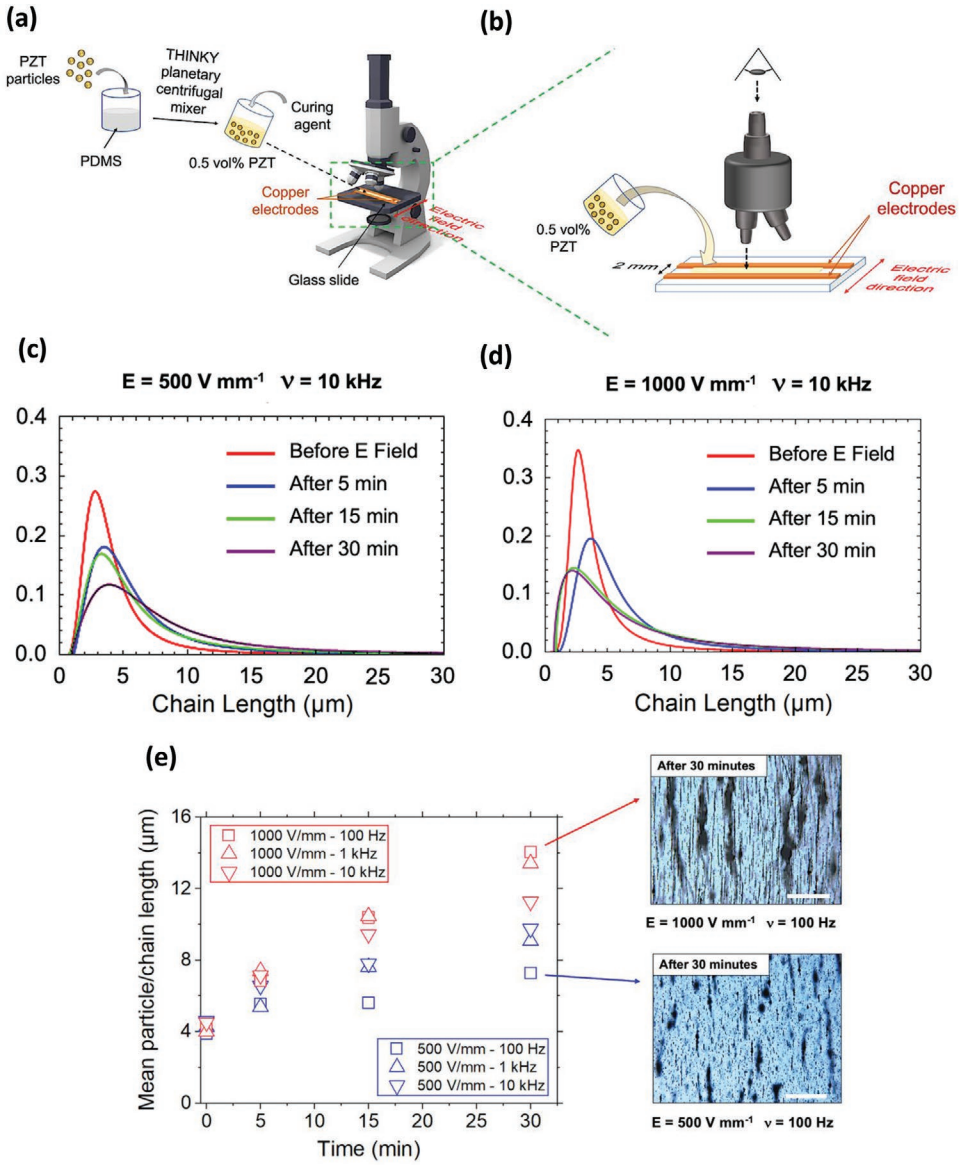

Figure 1. a) Schematic illustration of the solution fabrication process and b) the experimental setup for real-time investigation of in-plane alignment via optical microscope. c,d) The probability distribution functions of particles/chains at different time intervals for both (c) 500 V mm^{-1} and (d) 1000 V mm^{-1}, at 10 kHz. e) The mean particle/chain length (μm) versus time plots for six different experimental conditions. The optical images (captured after 30 min of electric-field exposure) show the effect of electric-field strength.

columns, where the light travels with little to no scattering or absorption. Therefore, as particles undergo induced polarization and create self-assembled chain-like structures, tracking the real-time light transmission can reveal significant information about the alignment mechanism. To this end, a custom-designed real-time measurement system was used to monitor the changes in light intensity while the sample was subjected to high voltage in the thickness ("Z") direction. The instrument consists of multiple sections and detectors: i) in-plane and out-of-plane birefringence measurement system, ii) laser displacement sensors (for real-time thickness measurements), iii) pyrometers, iv) light sources, v) hot air blower, vi) a wind tunnel with vertical baffles to control the uniformity of the air flow, v) high-voltage amplifier, vi) computerized balance (to monitor real-time changes in weight), vii) a universal serial bus (USB) camera, and viii) a UV light source. The schematic illustration of the instrument is shown in **Figure 2**a. More details about the real-time measurement system are provided elsewhere.[38] For this study, the transparent ITO-coated glasses were utilized as top and bottom electrodes. Before electric-field application, the PZT/PDMS mixtures were uniformly cast by a doctor blade onto the bottom electrode and four 2 mm thick glass spacers were then placed at the corner to provide an air gap between the electrodes (Figure 2a,b). Figure 2c shows the acquired real-time light transmission data during electric-field induced alignment of PZT samples with various particle loadings, ranging from 0.25 to 5 vol%. Before the electric-field application (time before 200 s), a steady flat line was recorded

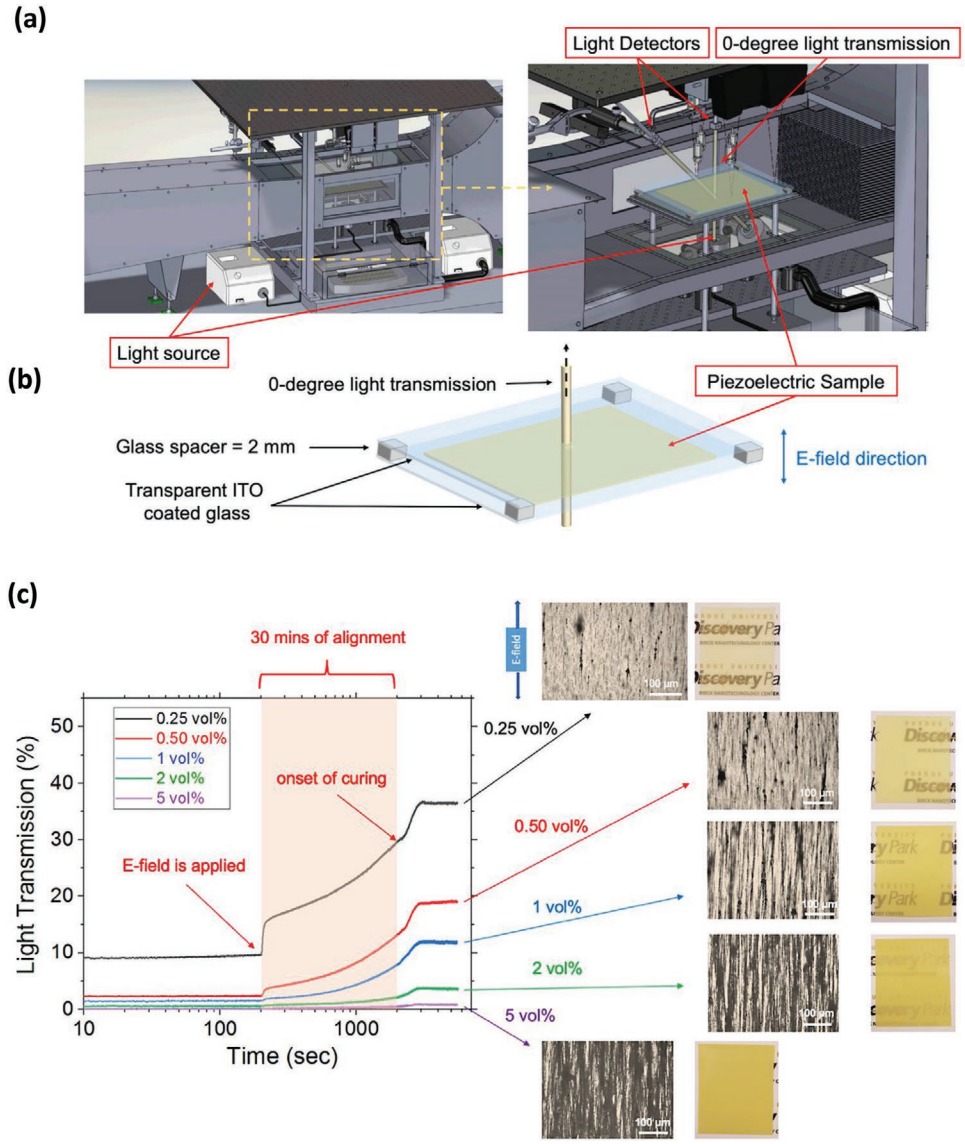

Figure 2. a) Schematic representation of the real-time custom-designed real-time measurement system which was used to monitor the changes in light intensity during external high-voltage application. b) The transparent ITO-coated glasses were utilized as top and bottom electrodes along with 2 mm thick glass spacers, which were placed at each corner to provide an air gap between the electrodes. c) The real-time light transmission data is shown at different stages of electric-field induced alignment for PZT samples with various particle loadings, ranging from 0.25 to 5 vol%. The optical microcopy images are also provided for each concentration (at 30 min) along with the photographs of the aligned films to demonstrate the change in optical transparency (scale bars: 100 µm).

for all concentrations, indicating no change in morphology. Additionally, in this time-window, light transmission decreased with increasing concentrations, which can be explained as the increased scattering or absorption by the additional particles. The initial sharp rise in the light transmission (upon the application of high voltage at 200 s) indicates the self-assembly of neighboring particles via the attractive electrostatic forces. The formed shorts chains then act as bigger dipole points and continue to attract smaller particles, which further broadens the depletion zones and increases the transparency. At his stage, the light transmission increases at a relatively slow rate (between 210 and 2000 s). After being exposed to electric field for 30 min, the temperature of the system was increased to 85 °C (at 2000 s) to freeze in the aligned morphology of the particles by thermal curing of surrounding resin. As can be noticed, during heating, the light transmission continues to grow slightly due to the temporary reduced viscosity of the polymer upon heating prior to curing induced rapid viscosity rise. This temporary reduction of viscosity, reduces the hydrodynamic resistance[39] (or viscous drag force (F_{drag})—given by Equation (4)) acting on each particle and thus, increases the mobility

$$F_{drag} = 6\pi\eta R\left(v_m - v_p\right) \tag{4}$$

where η is the viscosity, v_m and v_p are the velocities of the matrix and particle, respectively. At the end of the curing process, the

light transmission curves level off and remain flat. Figure 2c also shows the effect of change in concentration on particle orientation and pearl-chain formation. For instance, the transparency of the 0.25 vol% sample has risen up from 9% to 37%, whereas for 5 vol%, only a slight change was observed. This is because, at such high concentrations, spontaneously polarized particles cannot effectively orient their axes with the applied electric field due to the interruptions arising from the high spatial density of the adjacent particles. As a result, the distance between neighboring pearl chain columns (the width of depletion zone) decreases with increasing particle loading and thus, the transparency. The optical microcopy images are also provided for each concentration (at 30 min) along with the photographs of the aligned films to demonstrate the change in transparency level with varying concentrations (Figure 2c). Likewise, the cross-sectional micro-computed tomography (micro-CT) images verify the reduced depletion zone width between aligned columns at higher concentrations (**Figure 3**a). The spatial density analysis of the aligned PZT particles was also performed within the thickness range of 0–250 µm, starting from the bottom of the film. Figure 3b shows that at relatively low concentrations (i.e., between 0.25 and 1 vol%), the number of particles decreases rapidly as one proceeds from bottom to the top in the thickness direction of the aligned films. For example, in the case of 0.25 and 0.5 vol%, almost no particle was detected above 200 µm. However, at 2 vol%, the decrease in the spatial density was relatively slow compared to that of lower concentrations (Figure 3b,c), whereas between 5 and 13 vol%,

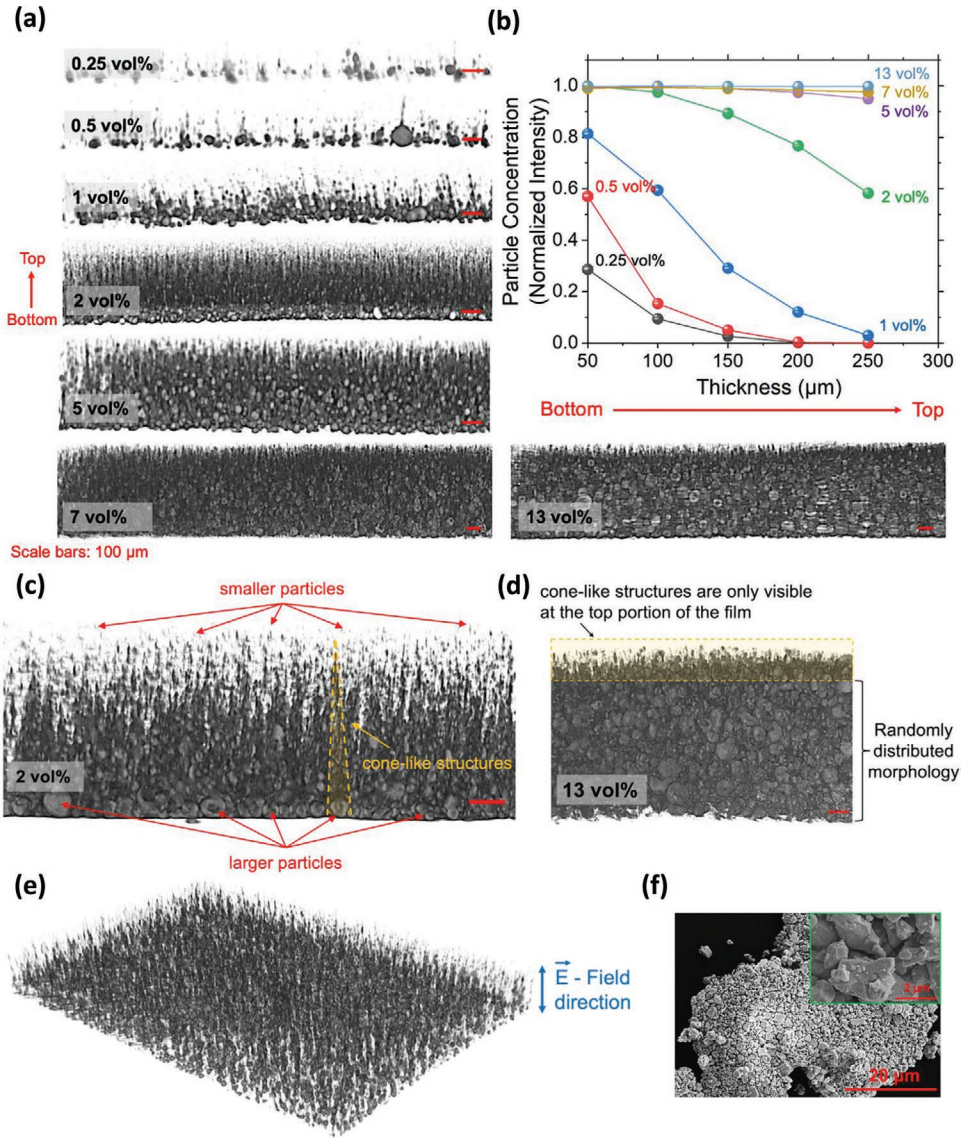

Figure 3. a) The cross-sectional microcomputed tomography (micro-CT) images of the aligned piezoelectric composites with different concentrations (i.e., between 0.25 and 13 vol%, scale bars: 100 µm). b) The spatial density analysis of the aligned PZT particles (within the thickness range of 0 to 250 µm, starting from the bottom of the film). c,d) High-resolution micro-CT images of (c) 2 vol% and (d) 13 vol% (scale bars: 100 µm). e) The aligned cone-like structures are shown via micro-CT from an oblique angle (5 vol% PZT). f) The SEM images of the larger particle clusters (scale bar: 20 µm). The inset image shows the small-sized particles (scale bar: 2 µm).

no significant variation was observed along the thickness direction. Finally, it is also noteworthy that, at 13 vol%, the anisotropic column-like structures were only visible at the portions close to the top surface, while the rest of the film exhibited a randomly distributed morphology due to congestion caused by the particles themselves (Figure 3d). Furthermore, as noticed in all micro-CT images, the aligned chains resemble cone-like structures rather than right cylindrical columns. This is due to the gravitational force (F_{grav}) acting on each particle (or particle clusters) during electric-field induced alignment. The F_{grav} depends heavily on the radius (R) of the particle and can be expressed by the following equation[39]

$$F_{grav} = -\frac{4}{3}\pi R^3 \left(\rho_P - \rho_m\right) g \tag{5}$$

where $\rho_m \cong 1$ g cm^{-3} and $\rho_P \cong 8$ g cm^{-3} are densities of the matrix and the PZT particle, respectively. The gravitational acceleration (g) is 9.81 m s^{-2}. According to Equation (5), the F_{grav} acting on a particle with a radius of 10 µm (≈287.6 pN) is three orders of magnitude greater than that of particle with a 1 µm radius (≈0.287 pN). As a result, as shown in Figure 3c, the larger particle clusters migrated toward the bottom of the film during the dielectrophoretic process and created the base portion of the cone. On the contrary, the relatively small particles were able to overcome the gravitational pull, which in turn gave rise to a particle size gradient along the formed chains. Figure 3e shows the aligned cone-like structures from an oblique angle. Furthermore, the scanning electron microscopy (SEM) images of the larger particle clusters along with the small-sized particles are provided in Figure 3f (the large image and the inset image, respectively).

2.2. Structural Configuration of Piezoelectric Force Sensors

After electric-field induced alignment of PZT particles and the thermal curing process, a stretchable and conductive silver-based ink was printed on both top and bottom surfaces of each sample. The copper strips were then placed on top of the printed silver electrodes and were used as electrical contacts for characterization measurements. In the final step, a thin layer (≈ 10 µm) of neat PDMS was cast as a protective layer (via a blade-coater) to encapsulate both the silver and the copper layers. The photograph and a schematic illustration of the sensor configuration are also provided in **Figure 4**a, where the magnified view shows the cross-sectional SEM image of the aligned PZT particles. Moreover, besides the PZT/PDMS systems, an aligned piezoelectric sample with a composition of 0.5 vol% PZT/0.02 vol% GNPs/PDMS was also prepared. The GNPs were introduced to facilitate the polarization and the charge transport by creating short conductive paths between PZT particles. This, in turn, reduces the overall internal resistance of the polymer-based composite and improves the piezoelectric output. Moreover, when the polarizability of the suspended particles (α_p), which in this case are GNPs, are much greater than the surrounding liquid medium (α_m), the electric-field lines become distorted at the particle–medium interface, creating stronger field intensities near the poles of the particles (Figure 4b).[40,41] As a result, the neighboring PZT particles form densely populated micrometer-sized columns around GNPs during dielectrophoretic organization. Figure 4c shows the micro-CT image of the PZT/GNPs/PDMS system, where the magnified SEM image reveals the interaction of GNPs with PZT particles under high voltage.

Since the conductive particles tend to polarize and align relatively fast in an external electric field compared to that of PZT particles, the exact volume fraction of the GNPs to be used was determined via a separate study, where different concentrations of graphene nanoplatelets were aligned in a PDMS resin at same field strength (1000 V mm^{-1}) and frequency (100 Hz) conditions to determine the percolation threshold. As shown in Figure S1 of the Supporting Information, 0.04 vol% was approximately the minimum concentration at which the graphene nanoplatelets formed multiple continuous electrical pathways from one electrode to the other. These columns, if isolated from the piezoelectric fillers, can adversely affect the piezoelectric properties by rendering the composite film electrically conductive and suppressing the net polarization in the thickness direction. Therefore, 0.02 vol% (just below the percolation threshold) was chosen as the optimum concentration to align the GNPs along with the PZT particles. More details about the aligned piezoelectric PZT/GNPs/PDMS system and as well as the effect of GNPs on the electromechanical output are provided elsewhere.[8] Likewise, similar observations have also been reported in different studies where randomly dispersed piezoelectric particles were mixed with graphitic fillers (e.g., single or multiwall carbon nanotubes, graphite, etc.) to improve the piezoelectric properties of the resulting composite.[13,42]

2.3. Characterization of Piezoelectric Coefficients (d_{33}, g_{33}) and Energy Harvesting Properties

Figure 4d shows the three different-sized samples (1 × 1 cm^2, 2 × 2 cm^2, and 3 × 3 cm^2) that were produced for applications including energy harvesting and structural health monitoring. The 2 × 2 cm^2 sized samples were utilized to characterize the piezoelectric charge and voltage coefficients (d_{33} and g_{33}) of the PZT/PDMS systems along with of the energy harvesting properties both aligned and random samples. To this end, a spherical steel ball with a 1 in. diameter was used as an impactor and was dropped onto the samples from four different heights to achieve four different impact force (i.e., 5.9 N, 8.3 N, 10.2 N, and 11.8 N) and pressure levels (i.e., 14.7, 20.8, 25.5, and 29.4 kPa). This method was adapted from Xu et al.[43] and Keawboonchuay and Engel.[44] The impact forces (F_{impact}) and the corresponding pressures were calculated by the momentum principle which is given by

$$F_{impact} = \frac{\Delta p}{\Delta t} \tag{6}$$

where Δt is the change in time (seconds) and Δp is the change in the momentum of the impactor which can defined as the product of mass (m) and change in velocity (ΔV)

$$\Delta p = m\Delta V = m\sqrt{2gh} \tag{7}$$

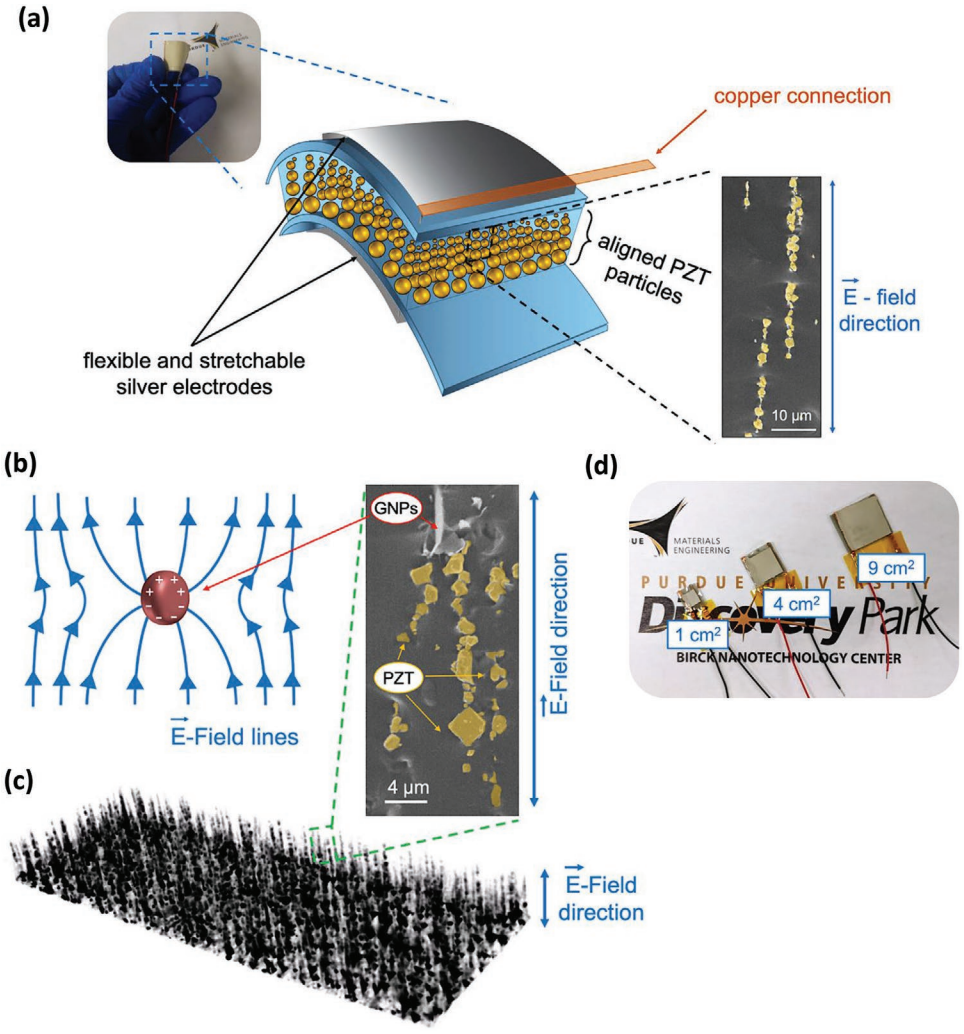

Figure 4. a) A photograph and a schematic illustration of the piezoelectric sensor configuration. The magnified view shows a cross-sectional SEM image of the aligned PZT particles along the electric-field direction (PZT particles are false colored to increase the contrast, scale bar: 10 μm). b) Schematic representation of the distorted electric-field lines around graphene nanoplatelets (GNPs)–polymer matrix interface, creating stronger field intensities near the poles of the particles. c) The micro-CT image of the PZT/GNPs/PDMS system, where the magnified SEM image reveals the interaction of GNPs with PZT under high voltage (PZT particles are false colored to increase the contrast, scale bar: 4 μm). d) The photograph of the three different sized samples (1×1 cm^2, 2×2 cm^2, and 3×3 cm^2).

where h is the drop height and g is the gravitational acceleration. Furthermore, in order to obtain uniform pressure distributions during impact test, samples were first sandwiched between two smooth aluminum disks (0.5 in. thick). Subsequently, the samples were then connected to a breadboard circuit setup where a voltage divider was composed of two 22 kΩ resistors. A single 22 kΩ resistor and the equivalent 44 kΩ resistance (both 22 kΩ resistors) were used to measure the current and the voltage output via an oscilloscope, respectively. The photograph and a schematic illustration of the experimental setup are provided in **Figure 5**a,b.

Figure 5c shows the typical pulse response obtained from piezoelectric samples upon impact, where the green line represents the voltage output measured across the equivalent 44 kΩ resistance. The current (I) output was calculated through the voltage measured across the 22 kΩ resistor (blue line) by using the Ohm's law

$$V = IR \tag{8}$$

where R is the resistance (Ω). The piezoelectric charge constants (d_{33}) were then obtained through the following equations[45]

$$d_{33} = \frac{Q}{F_{\text{impact}}} \tag{9}$$

$$Q = It \tag{10}$$

where Q is the generated charge (Coulomb) and t is the time duration (in seconds) that current flows in a circuit indicated with red dashed lines in Figure 5c. The output current and the corresponding d_{33} values were calculated at all impact force (F_{impact}) levels for each concentration and then averaged. As shown in **Figure 6**a, the dielectrophoretically aligned anisotropic samples were proven to exhibit higher piezoelectric charge constants (d_{33}) at relatively low particle loadings compared with that of randomly distributed composites. Moreover,

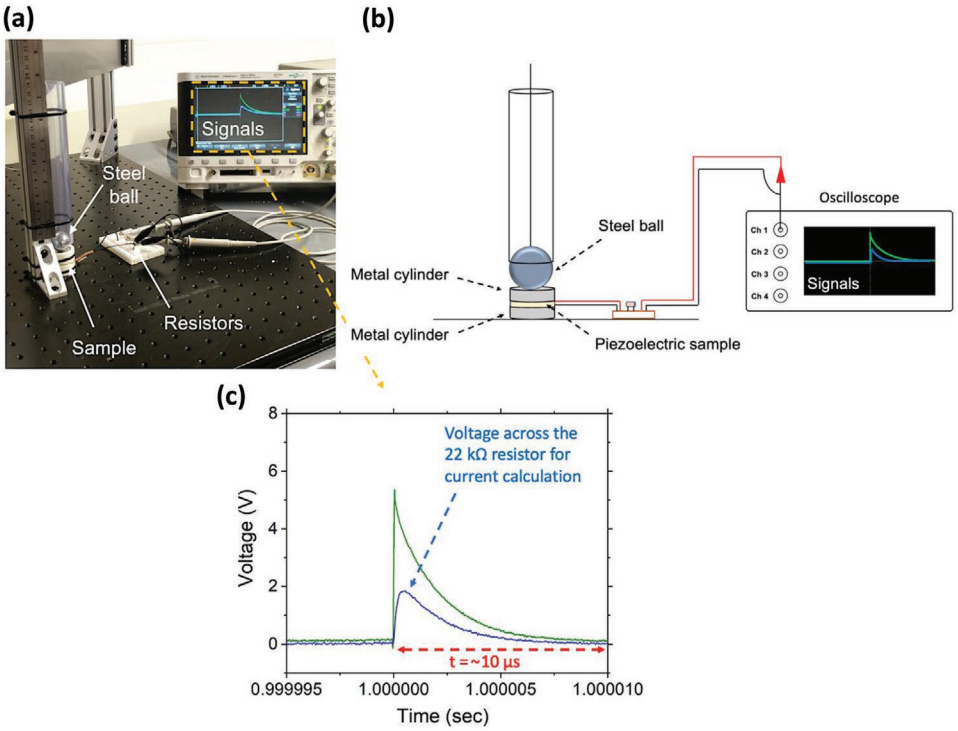

Figure 5. a) The photograph and b) a schematic illustration of the experimental setup used for energy harvesting. c) The typical pulse response obtained from piezoelectric samples upon impact, where the green line represents the voltage (*V*) output measured across the equivalent 44 kΩ resistance (both 22 kΩ resistors). The current (*I*) output was calculated through the voltage measured across the individual 22 kΩ resistor (blue line) by using the Ohm's law.

as denoted in the magnified view, the alignment of 0.02 vol% GNPs along with the 0.5 vol% PZT particles also significantly improves the d_{33} coefficient. After obtaining the d_{33} values, the piezoelectric voltage constants (g_{33}) were then calculated by the expression below

$$g_{33} = \frac{d_{33}}{\varepsilon} \tag{11}$$

Figure 6b plots the relative dielectric constants (ε) as a function of concentration and shows the enhancement in the permittivities with increased particle loading and orientation. An extraordinary g_{33} value of 0.709 Vm N^{-1} was recorded with an oriented 1 vol% PZT sample, and to the best of our knowledge, is ≈20% greater than the highest g_{33} reported in the literature (i.e., 0.6 Vm N^{-1}).[33] Starting at 2 vol%, the contrast between the dielectric constants of the oriented and the random samples increase with the increase in particle loading, which results in lower g_{33} values at higher concentrations (Figure 6c). Therefore, as reported in similar studies,[27,29] the piezoelectric voltage coefficients of the oriented PZT samples each exhibit a maximum at relatively low concentrations. Figure 6d shows the comparison of d_{33}, g_{33}, and ε_r values of different types of piezoelectric materials with the aligned PZT/PDMS systems of this work (the values obtained in this study are denoted with red and blue stars). After calculating the piezoelectric charge and voltage coefficients, the peak power output (P) for 4 cm^2 sized samples were then simply calculated from the raw output data (by obtaining V and I from the coinciding peaks of the voltage output and calculated current output, respectively) by the following equation

$$P = VI \tag{12}$$

Figure 6e shows the peak power densities calculated at 29.4 kPa for both aligned and random samples. As in the case of d_{33} coefficients, the results indicate that the aligned PZT samples also display higher power generation up to 2 vol% than that of their randomly distributed counterparts and can reach a maximum value of ≈2.5 mW cm^{-3}.

To demonstrate the sensitivity of the oriented systems, a 2×2 cm^2 area PZT/GNPs/PDMS sample was used to detect and monitor the locomotion of a small-sized insect. **Figure 7**a shows the photograph of a cricket placed on the top of a piezoelectric sensor and the oscilloscope baseline signal in the background. Initially, no signal was observed since there was no transient movement by the insect. However, when the cricket walked slightly to its left (Figure 7b), the movements were captured and monitored through the generated multiple voltage signals, corresponding to the forces exerted by each individual leg of the insect. Moreover, the signal intensities can also provide useful information about the magnitude of the forces applied. As shown in Figure 7c, the reduced intensity of the signals suggests that the insect had exerted relatively small forces during that time period of the test than before (Video S1, Supporting Information). This proof-of-concept experiment also demonstrates the capability of dielectrophoretically aligned samples to sense and thus, harvest energy from small biological and mechanical motion sources.

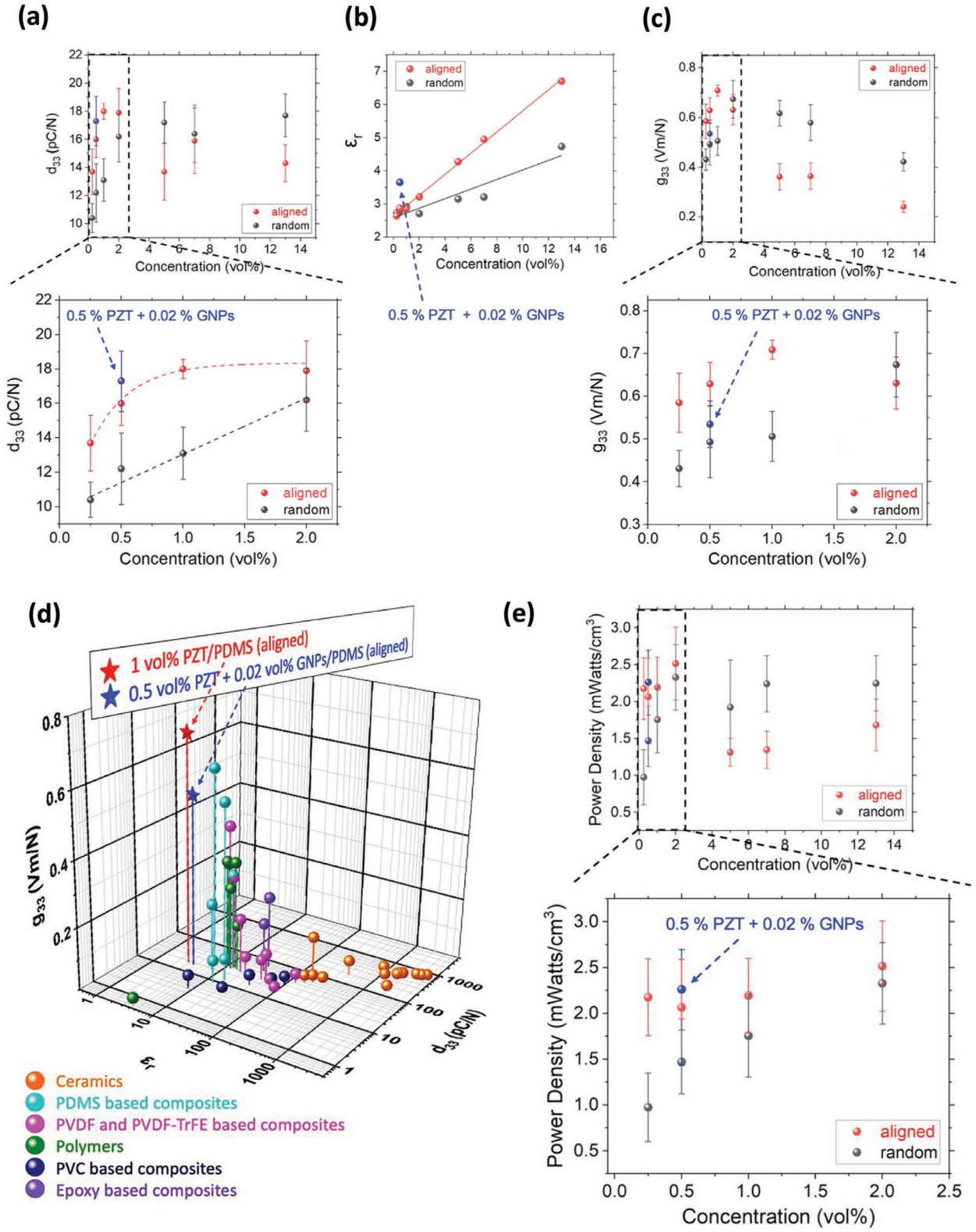

Figure 6. a) The piezoelectric charge coefficients (d_{33}), b) relative dielectric constants (ε_{33}), and c) the piezoelectric voltage coefficients (g_{33}) of both aligned and randomly distributed samples at different concentrations. d) Comparison of d_{33}, ε_r, and g_{33} values of different types of piezoelectric materials (the values obtained in this study are denoted with red and blue stars): (i) ceramics,[57–61] (ii) PDMS-based composites,[27,33,62–64] (iii) PVDF and PVDF-TrFE based composites,[65–67] (iv) PVC-based composites,[68] (v) epoxy-based composites,[69] and (vi) polymers.[9,59,61,70] e) Power-density output of both aligned and randomly distributed samples at different concentrations.

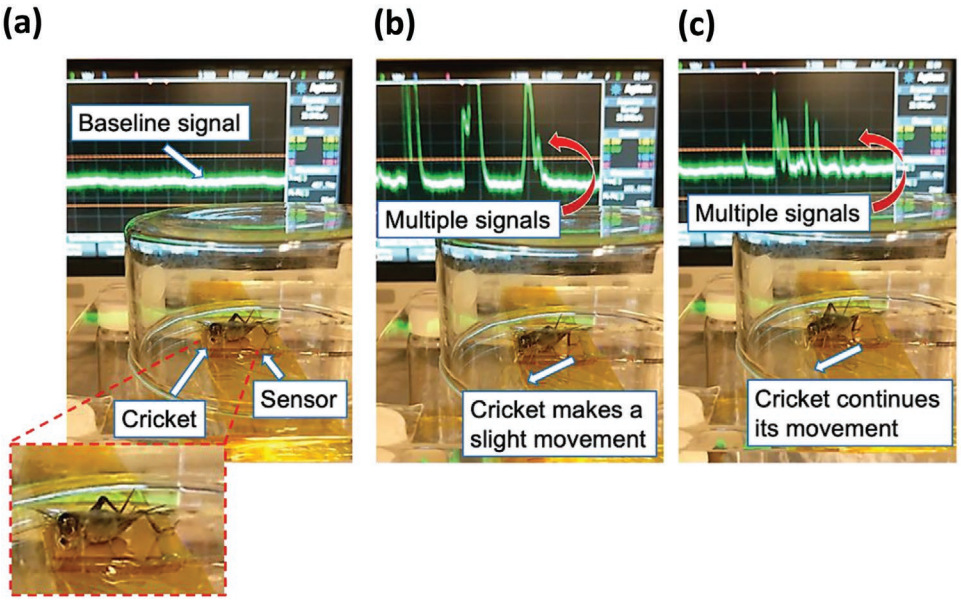

Figure 7. a) The photograph of a cricket placed on the top of a structured piezoelectric sensor (the oscilloscope baseline signal is also shown in the background). Initially, no signal was observed since there was no transient movement by the insect. b) When the cricket moves, it exerts force and hence, generates multiple voltage signals, corresponding to multiple individual legs of the insect. c) As the cricket continues its movement, the amplitudes of the signals change with fluctuating force levels.

2.4. Structural and Personal Health Monitoring

Besides their use for energy harvesting and impact sensing applications, piezoelectric sensors can be very useful for non-destructive structural health monitoring (SHM), where the continuous maintenance and the structural integrity of complex systems (e.g., engines and large machineries, aircrafts, buildings, bridges, pipelines, ships, etc.) are of major concern. In general, the SHM techniques are based on multiple sensor arrays. The previously reported studies[46–50] have shown that the process of real-time damage monitoring and performance evaluation requires sensors with well-defined characteristics such as high sensitivity, fast response time, and flexibility. To demonstrate the applicability and functionality of the electric-field aligned composite films, a 1×1 cm^2 sensor with a composition of 0.5 vol% PZT/0.02 vol% GNPs/PDMS was attached to a benchtop motor testbed to collect mechanical vibration signals for both normal and faulty conditions. Moreover, as shown in **Figure 8**a,b (side-view), a same-sized 0.5 vol% PZT/PDMS sensor (aligned) was also mounted to the same testbed as a control system to further investigate the effect of GNPs on the sensor performance.

First, when the motor was off, an initial baseline data was recorded across a frequency range of 0–500 Hz (Figure 8c). The motor was then powered by a 12 V DC power supply and run under a steady-state condition (i.e., constant rotational speed). Figure 8d shows the data acquired through the aligned PZT/GNPs/PDMS sample in steady state (normal mode), where multiple peaks were observed at various frequencies. Subsequently, these vibratory signals and the corresponding amplitudes were utilized as a reference to detect and analyze faulty conditions in the testbed. To simulate a faulty operation, two levels of misalignment were introduced by creating different degrees of shift in the centerline of the motor. The photographs of the misalignments and the respective frequency responses in each scenario are shown in Figure 8e–h. For example, in normal mode (no misalignment), the amplitudes of the signals detected at 400 Hz were relatively uniform and stable across all samplings. However, the same signals were significantly distorted when the centerline of the motor was tilted, indicating a problem in the continuous operation of the system (Figure 8e,f). In some samplings (at 400 Hz), these amplitudes were up to three times greater than those acquired in normal mode and were no longer uniform across the measurements. Similar trends were also observed in other frequencies. Likewise, when the degree of misalignment was increased (Figure 8g), a different signal profile was obtained in comparison to both normal and relatively small misalignment modes (Figure 8h). This capability to sense slight aberrations in frequency profiles at various modes along with its flexibility to conform to complex geometries make these materials a promising candidate for SHM applications. Finally, Figure S2a,b of the Supporting Information provides a side by side comparison of the aligned PZT/PDMS and PZT/GNPs/PDMS sensors in both normal and faulty conditions, respectively. As can be seen, in both modes, the sample with the GNPs was able to identify more distinct frequencies than the sample without GNPs and the signal amplitudes in some samplings were approximately an order of magnitude higher than that of the PZT/PDMS system. These results once again demonstrate the positive impact of GNPs on sensor performance but in this case in a vibratory environment.

In addition to complex machinery systems, the continuous monitoring and detection of abnormalities in the physiological signals (e.g., electrocardiogram signal, respiration rate, skin temperature, etc.) are also of importance, especially for

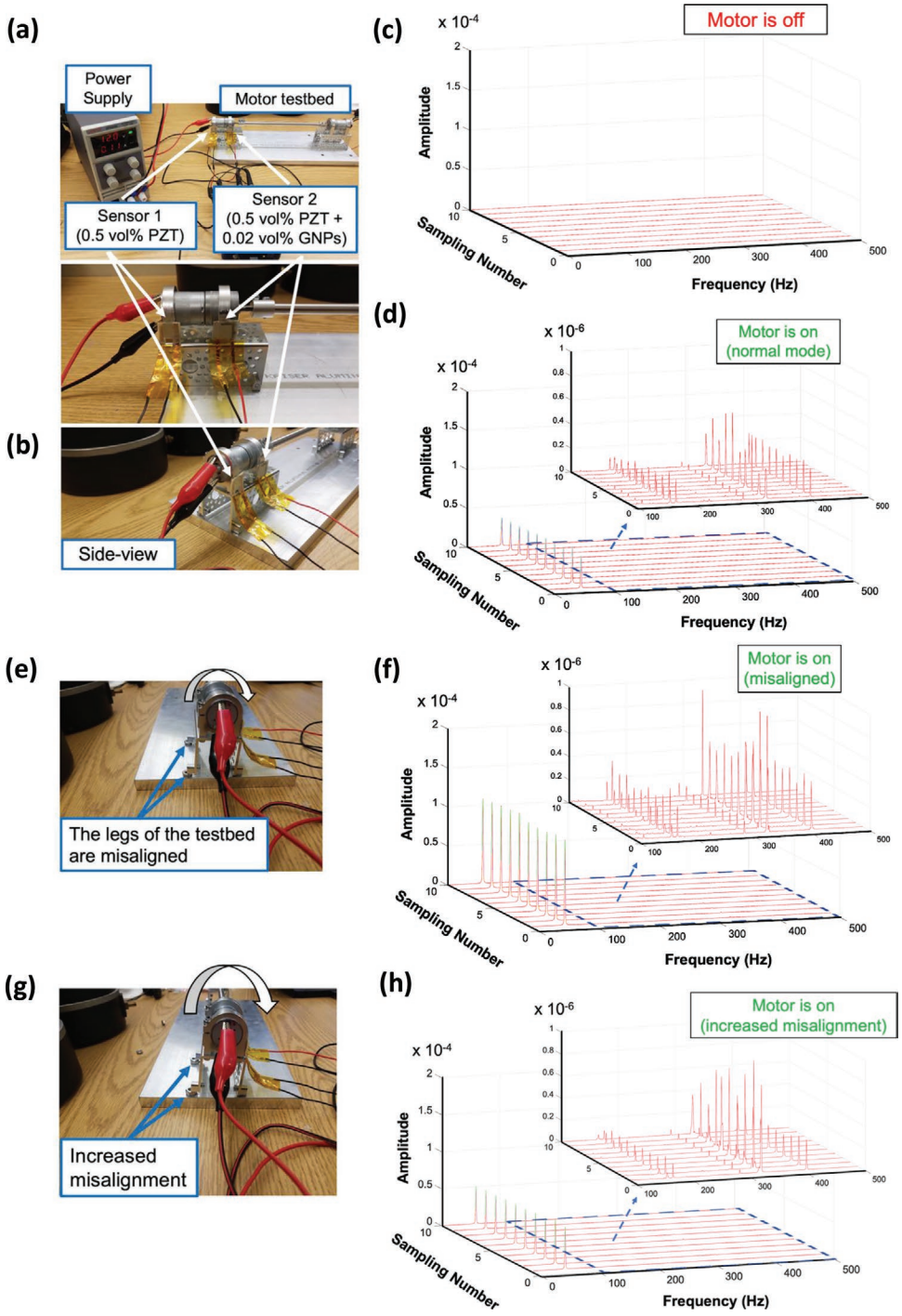

Figure 8. a) The experimental setup for structural health monitoring, where aligned 0.5 vol% PZT/PDMS and 0.5 vol% PZT/0.02 vol% GNPs/PDMS samples with 1 cm^2 active areas were mounted on a motor testbed to monitor the normal and faulty conditions in real time during its operation. b) The side-view of the motor testbed. c) When the motor was off, an initial baseline data was recorded across a frequency range of 0–500 Hz. d) Frequency versus amplitude response of the motor during normal operation mode (acquired via PZT/GNPs/PDMS system). e–h) The legs of the testbed were misaligned in order to create different degrees of shift in the centerline of the motor. (e) Misaligned motor and the corresponding (f) frequency versus amplitude response of the faulty motor (acquired via PZT/GNPs/PDMS system). (g) Increased misalignment and the corresponding (h) frequency versus amplitude response (acquired via PZT/GNPs/PDMS system).

early diagnosis and prevention of various health disorders in humans. Among these, the heart and the real-time analysis of its activity are regarded as key research areas since the recent studies strongly suggest that the heart-related diseases and complications are the leading cause of death among men and women worldwide.[51–53] These complications include

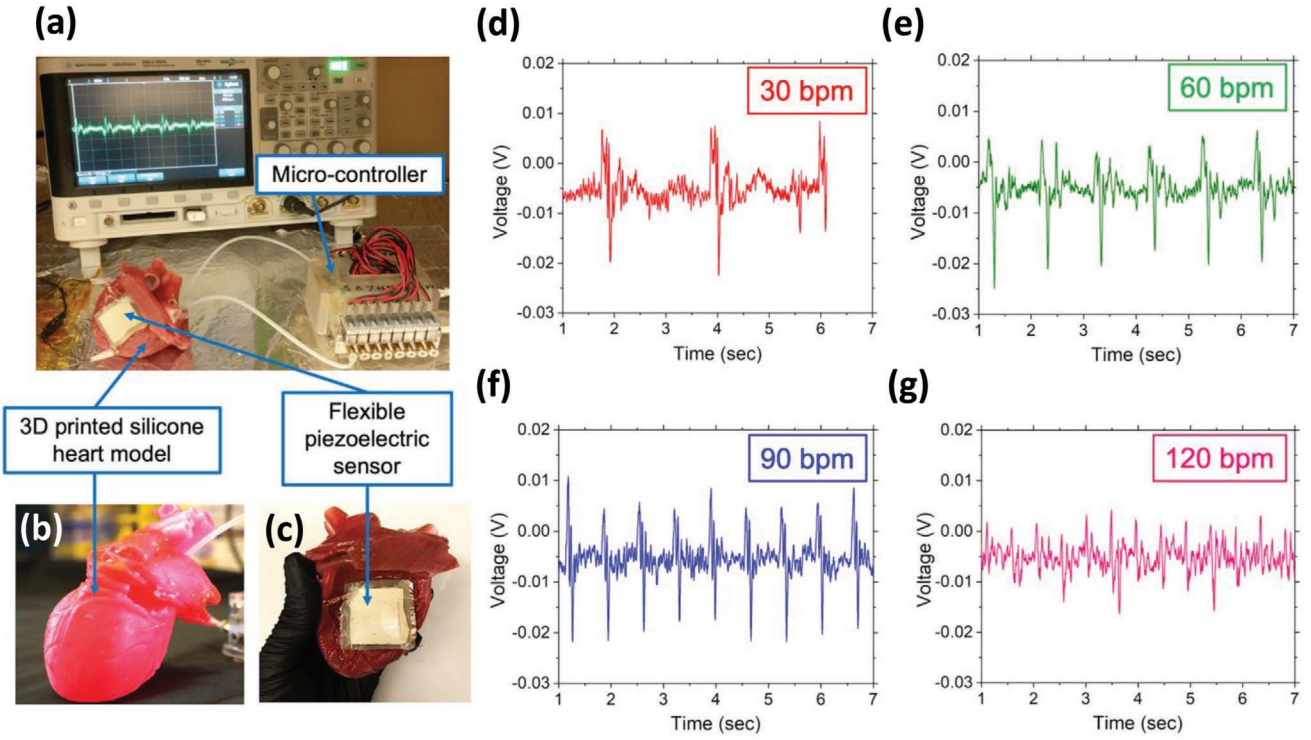

Figure 9. a) The experimental setup for personal health monitoring. b,c) The photograph of the silicone-based heart model. c) A 3×3 cm^2 piezoelectric sensor was used to monitor the actuation of the heart in real time at different frequencies: (d) at 30, (e) 60, (f) 90, and (g) 120 bpm.

myocardial infarction (also known as heart attack), congestive heart failure, and arrhythmia (irregular heartbeat). The cardiac arrhythmia occurs when the regular rhythm of the heart is disturbed, causing it to beat too fast (tachycardia), too slow (bradycardia) or irregularly.[54,55]

To study the performance of the flexible piezoelectric sensors in such heart-related diseases, an artificial physical model that mimics the anatomical features of the hearth was designed and molded (via a 3D printed mold) using a soft silicone-based elastomer Ecoflex. The photograph of the heart model is shown in **Figure 9**a–c. A 3×3 cm^2 sized flexible piezoelectric sensor was then adhered directly onto the top surface of the model via a thin layer of Sylgard 184. At the end of the thermal curing process of the thin layer, a robust and flexible interface was achieved between the heart model and the sensor. The actuation of the heart was regulated through a control unit with solenoid valves and an Arduino microcontroller board (Figure 9a). Although the control unit has multiple valves for both positive and negative pressures, for this research, only one valve was used to actuate the heart at various frequencies. Figure 9d–g shows the results obtained when the heart was actuated (Video S2, Supporting Information) at four different beats per minute (bpm) values: i) 30, ii) 60, iii) 90, and iv) 120 bpm. In a healthy human adult, the resting heart rate ranges between 60 and 100 bpm.[56]

As the acquired signals indicate, the flexible sensor was able to successfully respond to the changes in frequencies up to 120 bpm. Moreover, it is also noteworthy that the amplitude of the signals at 120 bpm was relatively small compared with the rest of the bpm levels. This is because, at higher bpm, the heart model does not inflate and stretch as much as it does at small bpm values. As a result, the force that the heart exerted on the sensor was reduced.

2.5. Large-Area Film Production via Continuous Roll-to-Roll (R2R) Electric-Field Alignment

Finally, to demonstrate the scalability of the electric-field induced alignment, a 44 ft long novel custom-designed R2R manufacturing line was utilized. As shown in the schematic illustration (**Figure 10**a), the line is made up of multiple, separate processing modules and sections: i) unwinding and solution casting station (via doctor blade, slot-die or flow coating), ii) electrospinning chamber (contains nine individual nozzles), iii) single screw extruder for melt casting, iv) high voltage electric-field alignment zone, v) individual heating plates, and vi) high power laser for thermal processing, vii) magnetic-field alignment zone (maximum magnetic field strength: 2.7 T), viii) UV curing ix) photonic curing module (PulseForge 1200), which uses pulsed light generated via a xenon flash lamp, x) heating ovens, and xi) rewinding section. In addition, the custom-design nature of the production line enables different modules to be combined and used simultaneously for different applications in a class 100 cleanroom environment. For this work, the doctor-blade solution-casting station was used along with the high-voltage electric-field module and nine individual heating plates (located under the top copper electrode along the casting direction—Figure 10b). First, a piezoelectric solution with a composition of 0.5 vol% PZT/0.02 vol% GNPs/PDMS

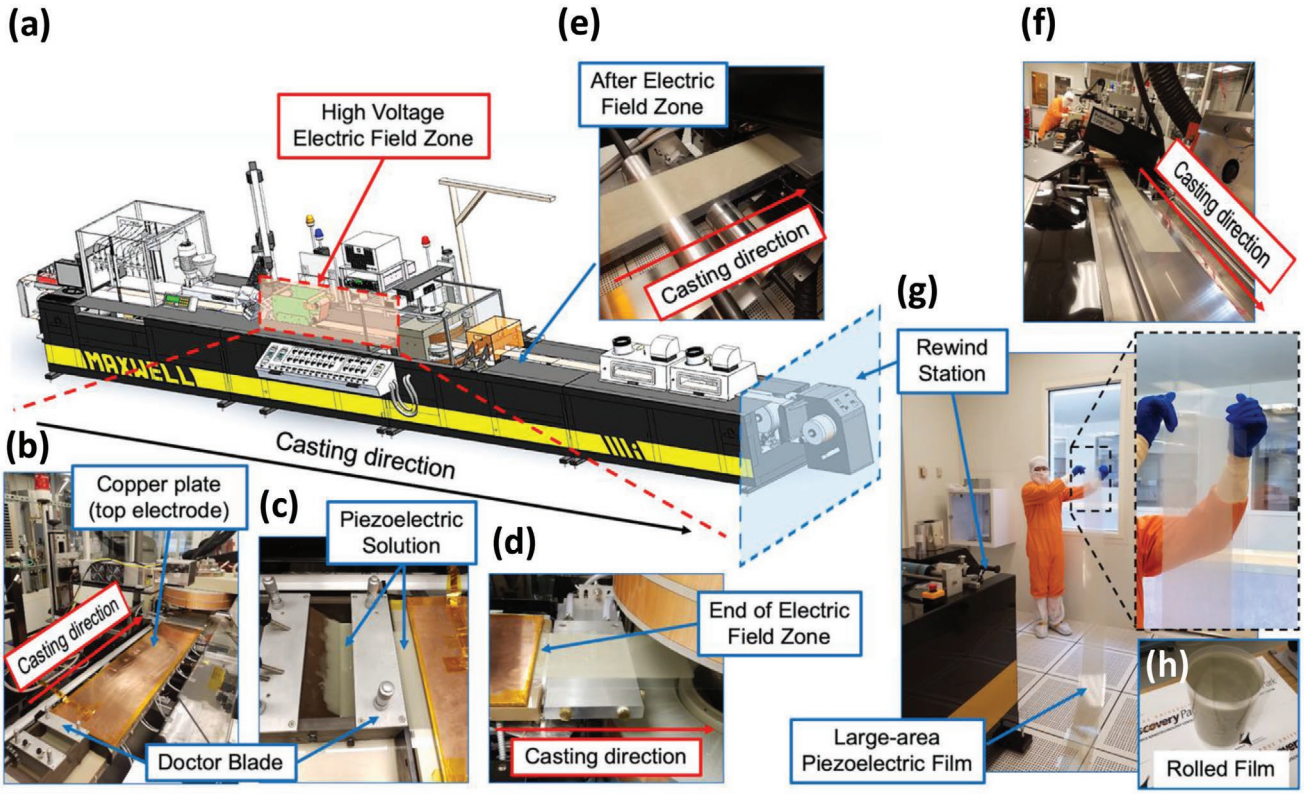

Figure 10. a) The schematic illustration of the custom-designed multifunctional roll-to-roll (R2R) manufacturing line (actual length of the line: 44 ft). Reproduced with permission.[8] Copyright 2019, Wiley-VCH. b–d) High-voltage electric-field zone. (b) A flat copper plate was used as a top electrode during continuous electric-field alignment (the individual heating plates were located under the top electrode, along the casting direction). (c) The piezoelectric solution was uniformly cast on a flexible and transparent 8-in.-wide PET substrate via a 6-in.-wide doctor blade. (d) The aligned piezoelectric film leaves the high-voltage zone. At this stage the film was fully cured and hence, the aligned columns were frozen into place. e,f) The aligned film is being carried to the rewind station of the line. g) A 12 ft long and a 6-in.-wide sample was obtained at the end of the process. h) The photograph of the rolled film.

was prepared and mixed via a THINKY planetary centrifugal mixer (the curing agent was also introduced with a base-to-agent ratio of 10:1). As shown in Figure 10c, the solution was then uniformly cast on a flexible and transparent 8-in.-wide PET substrate via a 6-in.-wide doctor blade. Subsequently, the solution was continuously carried into the high voltage electric field zone and exposed to an external AC electric field with a field strength of 1000 V mm^{-1} (frequency: 100 Hz). At this stage, during dielectrophoretic alignment, the first five heating plates were kept at room temperature to prevent the precuring of the matrix. This in turn provides the sufficient mobility and the necessary time to the particles by keeping the viscosity of the solution relatively low at the early phase of alignment process. The remaining four heating plates were set to higher temperature values ranging between 75 and 90 °C (with 5 °C increments). This gradual increase in temperature provides an extra mobility to the particles at the initial stage of the thermal curing process by further reducing the viscosity (explained in Section 2.1). In the final stage, the viscosity of the solution increases with increasing temperature and fully cures before it exits the electric field zone, freezing in all micro- and nano-columnar structures along the thickness direction (Figure 10d). Figure 10e,f shows the photographs of the structured piezoelectric film being carried to the rewind station of the line. At the end of the roll-to-roll process, a 12 ft long and a 6-in.-wide film was collected (Figure 10g). To the best of our knowledge, this is the largest single piece piezoelectric film ever reported in the literature. Figure 10h also displays the film in a rolled form.

3. Conclusions

The flexible quasi 1–3 piezoelectric composites were produced by the dielectrophoretic alignment of micro- and nanosized PZT particles in a polydimethylsiloxane (PDMS) matrix. The novel piezoelectric material produced exhibited a record-high piezoelectric voltage coefficient (g_{33}) of 0.709 Vm N^{-1}, ≈20% greater than the highest g_{33} value reported in the literature.[57–70] The piezoelectric and dielectric properties of both aligned and random samples were characterized at various different concentrations along with their light transmission and morphological characteristics. Moreover, the effects of graphitic particles on piezoelectric properties were also investigated by the alignment of small volume fraction of graphene nanoplatelets together with PZT particles. The fabricated high-performance films were then used to demonstrate the potential applications of these structured composites in various areas such as energy harvesting, low impact force detection, and structural and

personal health monitoring. Finally, to show the scalability of the process, a large-area (12 ft long and 6-in.-wide) sample was also manufactured via a continuous dielectrophoresis process utilizing a novel 44 ft long custom designed multifunctional R2R manufacturing line, resulting in the largest single piece piezoelectric film ever reported in the literature. Furthermore, the R2R production can further extend and open up new potential application areas, where conformable large area samples are needed for nonflat surfaces.

4. Experimental Section

Fabrication of Quasi 1–3 Composites: The PZT/PDMS samples are two-phase systems. The PZT (NCE55) was obtained as a powder from Noliac. Large agglomerations were reduced manually with a mortar and pestle. The resulting powder was sieved to control the particle size distribution. The PDMS (Sylgard 184) resin was obtained from Dow and was used as received. The polymer was loaded with 0.25, 0.5, 1, 2, 5, 7, and 13 vol% PZT to form the composite film. For the three-phase PZT/GNPs/PDMS system, the GNPs were obtained from Sigma-Aldrich and were used as received. The polymer was loaded with 0.5 vol% PZT and 0.02 vol% GNPs. For all samples, the particle phases were first dispersed in the prepolymer using a planetary centrifugal mixer (THINKY Mixer, ARE-310). Then, the curing agent was then added in the 10:1 weight ratio of the thermocurable resin and again dispersed using the centrifugal mixer. To further improve the homogeneity of the dispersion, the material at the walls and bottom of the mixing container were manually stirred back into the bulk before briefly remixing it in the centrifugal mixer. The suspension was immediately cast using the doctor-blade method on an ITO-coated glass substrate (SPI Supplies) to mitigate sedimentation. A second ITO-coated glass plate was used as the top electrode. 2 mm thick glass spacers were placed between the two electrodes to maintain an air gap and ensure uniform field strength across the sample during the alignment process directly after casting. To apply AC electric field, a waveform generator, connected to a high-voltage amplifier (AMP-20B20-LC, Matsusada), applied a sinusoidal voltage to the electrodes (peak-to-peak field strength: 1000 V mm^{-1}, 100 Hz).The electric field was maintained continuously until curing was complete. The resulting freestanding films were cut to size (1×1 cm^2, 2×2 cm^2, 3×3 cm^2) and coated with electronic ink (DuPont, Intexar Pe874). A strip of copper tape was attached to each side of the samples to create electrical interconnects. The stretchable silver ink was overcoated with a thin layer of PDMS to increase its durability.

micro-CT: The morphology of the structured aligned PZT/PDMS and PZT/GNPs/PDMS was imaged with a desktop micro-CT system (Bruker Skyscan 1272). The 2D shadow projections from the scanner were recorded at a resolution of 7.4 µm per pixel. For concentrations below 13 vol%, the X-ray source energy was set to 80 kV/125 µA and the beam was selectively hardened with a 1 mm thick Al filter. The specimens were rotated over 180° of rotation at steps of 0.4°. Due to the increased electron density, the 13 vol% sample was scanned at 100 kV/100 µA, using a 0.11 mm Cu filter at 0.2° rotation steps over 180°. Frame averaging was utilized to increase the signal-to-noise-ratio. For each sample, virtual slices were then reconstructed in NRecon (version 1.7.1.0) from the radiographs. 3D models were created in CTVox by volume rendering the cross-sections. Regions of high electron-density were assigned greater opacity in the regenerated volume to feature the PZT particles.

SEM: To visualize the morphology of the structured samples, the cross-section was imaged with a field emission scanning electron microscope (Hitachi S4800). To prepare the specimen, the film was submerged in liquid nitrogen and fractured, resulting in a smooth cross-sectional surface. Then, a conductive Pt–Au top layer was applied to the specimen surface by sputter coating (SPI-Module Sputter Coater) in an argon atmosphere.

Output Voltage (V) and Current (I) Measurement: To characterize the power output of the composites (2×2 cm^2 active area), the samples were subjected to a drop weight impact to provide a dynamic force. A 1 in. diameter steel ball (Thomas Scientific) was dropped from a series of heights (1, 2, 3, and 4 in.), producing different energy levels. To guide the drop-weight path, a clear PVC pipe (pipe size: 1, Schedule 40) was mounted to a T-slot aluminum rail (1 in. rail height). The rail was then vertically mounted to an optical breadboard (Thorlabs). To create a uniform pressure from the point-like impact force, two smooth aluminum disks (multipurpose 6061 aluminum, diameter: 1 in., length: 0.5 in.) were used to sandwich the samples. The disks were held in separate PVC pipe sleeves to constrain their motion to the vertical direction. A small gap was left between the pipe sleeves and the drop-guide pipe to prevent a cushion of air from forming. The sample was then loaded by a circuit with two 22 kΩ resistors in series on a solderless breadboard. Two oscilloscope probes read the voltage across both resistors (equivalent to the voltage across the sample, acting as the source) and one resistor, respectively. The latter resistor was used to calculate current according to Ohm's law. The peak recorded voltage values were used in all cases, as recorded by an oscilloscope (DSOX3034A, Agilent Technologies).

Structural Health Monitoring: A benchtop motor testbed was constructed to collect mechanical vibration signals in rotating machinery using PZT/PDMS and PZT/GNPs/PDMS-based sensors with 1×1 cm^2 active areas. In the testbed, a general motor–generator setting was implemented, with one power and one load motor. Two DC motors (no. 638 350, Actobotics) were used, connected by a stainless-steel shaft (diameter: 8 mm, length: 200 mm). A rigid base (6061 aluminum flat plate, length: 355.6 mm, width: 152.4 mm, height: 12.7 mm) secured each motor through the same series of components. At the bottom of each mount, four brackets were screwed into holes that were drilled to precisely align the centerlines of the motor output shafts parallel. To achieve this, the flat base plate was machined with a computer numerical control machine. The brackets held the fringes of an aluminum channel with pins at each corner. Two clamping mounts, one for each end of the motor, were screwed into the top of the aluminum channel. In the testbed, two levels of misalignment were introduced by creating different degrees of shift in the power motor's centerline. To this end, two sizes of hex nuts (level 1: M3 hex nut, level 2: M6 hex nut) were added along one fringe as spacers between the bracket and the base plate.

Fabrication of the 3D Printed Heart Model: The heart model was designed not to have internal features for ease of actuation. The external anatomical features of the heart were designed using CAD software (Fusion 360) for use as a negative mold. The heart design was divided into three separate stages for ease of fabrication. The stages were approximate cross-sections, comprising the ventricles, the atria, and the major blood vessels. The three parts were 3D printed using PLA filament (Raise3D Premium PLA Filament) in a fused-filament fabrication 3D printer (Raise3D Pro2 Plus). To fabricate a soft elastomeric model, the flat surface of each printed part was first sealed on a flat substrate. Then, addition-cure silicone rubber (Ecoflex 00–30) was applied to the interior of each negative mold using the layer-by-layer painting technique. Three layers of elastomer were cured in between coats at 30 °C for 20 min before removal. The silicone-rubber parts were sealed together with additional silicone rubber to form the hollow actuated heart model.

Actuating the Heart Model: To actuate the heart, a valve control unit was developed with solenoid valves and an Arduino microcontroller. The board was operated by a program written in the Arduino software integrated development environment and uploaded via USB. The controller was supplied by positive and negative-pressure lines and delivered pressure to connected devices by opening and closing valves. For the current project, one pair of valves was used, but the controller has the capacity for eight different devices with eight pairs of valves. The elastomeric heart model was connected to the controller using polyethylene tubing (inner diameter: 1/16 in., outer diameter: 1/8 in.) that was inserted into a slit in the model. The controller simulated a heartbeat by opening and closing both pressure valves for each cycle at a specified frequency.

Supporting Information

Supporting Information is available from the Wiley Online Library or from the author.

Acknowledgements

This research was funded by the startup funds of MC at Purdue, for which the authors are grateful.

Conflict of Interest

The authors declare no conflict of interest.

Keywords

dielectrophoresis, energy harvesting, flexible sensors, piezoelectric films, roll-to-roll manufacturing

Received: June 8, 2020
Revised: August 3, 2020
Published online:

[1] J. F. Tressler, *Piezoelectric and Acoustics Materials for Transducer Applications*, Springer US, Boston, MA **2008**, pp. 217–239.
[2] M. Martins, V. Correia, J. M. Cabral, S. Lanceros-Mendez, J. G. Rocha, *Sens. Actuators, A* **2012**, *184*, 141.
[3] E. T. Falangas, J. A. Dworak, S. Koshigoe, *IEEE Control Syst.* **1994**, *14*, 34.
[4] G. Bohannan, H. Schmidt, D. Brandt, M. Mooibroek, *Ferroelectrics* **1999**, *224*, 211.
[5] P. K. Panda, in *Aerospace Materials and Material Technologies, Aerospace Materials*, Vol. *1* (Eds: P. N. Eswara, R. J. H. Wanhill), Springer Singapore, Singapore **2017**, pp. 501–518.
[6] Z. Zhang, C. Yao, Y. Yu, Z. Hong, M. Zhi, X. Wang, *Adv. Funct. Mater.* **2016**, *26*, 6760.
[7] J. Yan, Y. G. Jeong, *ACS Appl. Mater. Interfaces* **2016**, *8*, 15700.
[8] A. Yildirim, R. Rahimi, S. Shams Es-haghi, A. Vadlamani, F. Peng, M. Oscai, M. Cakmak, *Adv. Mater. Technol.* **2019**, *4*, 1800425.
[9] S. Mishra, L. Unnikrishnan, S. K. Nayak, S. Mohanty, *Macromol. Mater. Eng.* **2019**, *304*, 1800463.
[10] K. Il Park, C. K. Jeong, N. K. Kim, K. J. Lee, *Nano Convergence* **2016**, *3*, 12.
[11] S. H. Shin, Y. H. Kim, M. H. Lee, J. Y. Jung, J. Nah, *ACS Nano* **2014**, *8*, 2766.
[12] S. Gupta, R. Bhunia, B. Fatma, D. Maurya, D. Singh, Prateek, R. Gupta, S. Priya, R. K. Gupta, A. Garg, *ACS Appl. Energy Mater.* **2019**, *2*, 6364.
[13] K. Il Park, C. K. Jeong, J. Ryu, G. T. Hwang, K. J. Lee, *Adv. Energy Mater.* **2013**, *3*, 1539.
[14] H. Li, C. Tian, Z. D. Deng, *Appl. Phys. Rev.* **2014**, *1*, 041301.
[15] C. R. Bowen, H. A. Kim, P. M. Weaver, S. Dunn, *Energy Environ. Sci.* **2014**, *7*, 25.
[16] D. Ponnamma, H. Parangusan, A. Tanvir, M. A. A. AlMa'adeed, *Mater. Des.* **2019**, *184*, 108176.
[17] X. Niu, W. Jia, S. Qian, J. Zhu, J. Zhang, X. Hou, J. Mu, W. Geng, J. Cho, J. He, X. Chou, *ACS Sustainable Chem. Eng.* **2019**, *7*, 979.
[18] A. Proto, M. Penhaker, S. Conforto, M. Schmid, *Trends Biotechnol.* **2017**, *35*, 610.
[19] J. Rao, Z. Chen, D. Zhao, Y. Yin, X. Wang, F. Yi, *Sensors* **2019**, *19*, 2763.
[20] W. Deng, T. Yang, L. Jin, C. Yan, H. Huang, X. Chu, Z. Wang, D. Xiong, G. Tian, Y. Gao, H. Zhang, W. Yang, *Nano Energy* **2019**, *55*, 516.
[21] S. S. Indira, C. A. Vaithilingam, K. S. P. Oruganti, F. Mohd, S. Rahman, *Nanomaterials* **2019**, *9*, 773.
[22] R. E. Newnham, D. P. Skinner, L. E. Cross, *Mater. Res. Bull.* **1978**, *13*, 525.
[23] L. Li, S. Zhang, Z. Xu, F. Wen, X. Geng, H. J. Lee, T. R. Shrout, *J. Phys. D: Appl. Phys.* **2013**, *46*, 165306.
[24] Q. Huang, H. Wang, S. Hao, C. Zhong, L. Wang, *Sensors* **2019**, *19*, 4336.
[25] Y. Li, G. Lu, J. J. Chen, J. C. Jing, T. Huo, R. Chen, L. Jiang, Q. Zhou, Z. Chen, *Photoacoustics* **2019**, *15*, 100138.
[26] S. A. Wilson, R. W. Whatmore, *Electric Field Structuring of Piezoelectric Composite Materials*, Cranfield University, UK **1999**.
[27] V. L. Stuber, D. B. Deutz, J. Bennett, D. Cannel, D. M. de Leeuw, S. van der Zwaag, P. Groen, *Energy Technol.* **2019**, *7*, 177.
[28] J. M. Yun, J. H. Shin, J. Ryu, N. M. Shinde, K. H. Kim, *Adv. Sustainble Syst.* **2018**, *2*, 1700133.
[29] D. A. Van Den Ende, B. F. Bory, W. A. Groen, S. Van Der Zwaag, *J. Appl. Phys.* **2010**, *107*, 024107.
[30] C. Hu, L. Cheng, Z. Wang, Y. Zheng, S. Bai, Y. Qin, *Small* **2016**, *12*, 1315.
[31] V. Tomer, C. A. Randall, *J. Appl. Phys.* **2008**, *104*, 074106.
[32] D. A. Van Den Ende, S. E. Van Kempen, X. Wu, W. A. Groen, C. A. Randall, S. Van Der Zwaag, *J. Appl. Phys.* **2012**, *111*, 124107.
[33] X. Gao, M. Zheng, X. Yan, J. Fu, Y. Hou, M. Zhu, *Nanoscale* **2020**, *12*, 5175.
[34] H. Tang, Y. Lin, H. A. Sodano, *Adv. Energy Mater.* **2012**, *2*, 469.
[35] R. Pethig, *Dielectrophoresis: Theory, Methodology and Biological Applications*, John Wiley & Sons, Inc, New York **2017**, pp. 31–48.
[36] R. Pethig, *Dielectrophoresis: Theory, Methodology and Biological Applications*, John Wiley & Sons, Inc, New York **2017**, pp. 119–144.
[37] F. J. Massey, *J. Am. Stat. Assoc.* **1951**, *46*, 68.
[38] E. Unsal, J. Drum, O. Yucel, I. I. Nugay, B. Yalcin, M. Cakmak, *Rev. Sci. Instrum.* **2012**, *83*, 025114.
[39] M. Nikolic-Jaric, S. F. Romanuik, G. A. Ferrier, T. Cabel, E. Salimi, D. B. Levin, G. E. Bridges, D. J. Thomson, *Biomicrofluidics* **2012**, *6*, 024117.
[40] A. D. Goater, R. Pethig, *Parasitology* **1999**, *117*, 177.
[41] S. Williams, in *Encyclopedia of Microfluidics and Nanofluidics* (Ed: D. Li), Springer US, Boston, MA **2013**, pp. 1–12.
[42] K. Il Park, M. Lee, Y. Liu, S. Moon, G. T. Hwang, G. Zhu, J. E. Kim, S. O. Kim, D. K. Kim, Z. L. Wang, K. J. Lee, *Adv. Mater.* **2012**, *24*, 2999.
[43] C. N. Xu, M. Akiyama, K. Nonaka, T. Watanabe, *IEEE Trans. Ultrason. Ferroelectr. Freq. Control* **1998**, *45*, 1065.
[44] C. Keawboonchuay, T. G. Engel, *IEEE Trans. Ultrason. Ferroelectr. Freq. Control* **2003**, *50*, 1377.
[45] Z. Sun, X. Zhang, Z. Xia, X. Qiu, W. Wirges, R. Gerhard, C. Zeng, C. Zhang, B. Wang, *Appl. Phys. A* **2011**, *105*, 197.
[46] G. Park, C. R. Farrar, F. L. Di Scalea, S. Coccia, *Smart Mater. Struct.* **2006**, *15*, 1673.
[47] X. Zhao, H. Gao, G. Zhang, B. Ayhan, F. Yan, C. Kwan, J. L. Rose, *Smart Mater. Struct.* **2007**, *16*, 1208.
[48] J. B. Ihn, F. K. Chang, *Smart Mater. Struct.* **2004**, *13*, 609.
[49] H. Gullapalli, V. S. M. Vemuru, A. Kumar, A. Botello-Mendez, R. Vajtai, M. Terrones, S. Nagarajaiah, P. M. Ajayan, *Small* **2010**, *6*, 1641.
[50] H. Gu, Y. Zhao, M. L. Wang, *Struct. Control Health Monit.* **2005**, *12*, 329.
[51] K. Mc Namara, H. Alzubaidi, J. K. Jackson, *Integr. Pharm. Res. Pract.* **2019**, *8*, 1.
[52] N. J. Pagidipati, T. A. Gaziano, *Circulation* **2013**, *127*, 749.

[53] A. N. Nowbar, M. Gitto, J. P. Howard, D. P. Francis, R. Al-Lamee, *Circ. Cardiovasc. Qual. Outcomes* **2019**, *12*.
[54] C. Ye, M. T. Coimbra, B. V. K. Vijaya Kumar, *Proc. of the 2010 Annual Int. Conf. of the IEEE Engineering in Medicine and Biology Society (EMBC'10)*, Buenos Aires, Argentina **2010**, pp. 1918–1921.
[55] D. Fu, *Cell Biochem. Biophys.* **2015**, *73*, 291.
[56] S. Das, S. Pal, M. Mitra, *J. Med. Eng. Technol.* **2017**, *41*, 170.
[57] Y. Yan, J. E. Zhou, D. Maurya, Y. U. Wang, S. Priya, *Nat. Commun.* **2016**, *7*, 13089.
[58] T. Suwannasiri, A. Safari, *J. Am. Ceram. Soc.* **1993**, *76*, 3155.
[59] A. Jain, K. J. Prashanth, A. K. Sharma, A. Jain, R. P. N. Rashmi, *Polym. Eng. Sci.* **2015**, *55*, 1589.
[60] H. I. Schlaberg, J. S. Duffy, *Sens. Actuators, A* **1994**, *44*, 111.
[61] Y. Kim Hyunuk, T. P. Shashank, *Energy Harvesting Technologies*, Springer US, Boston, MA **2009**, pp. 3–39.
[62] M. Wu, T. Zheng, H. Zheng, J. Li, W. Wang, M. Zhu, F. Li, G. Yue, Y. Gu, J. Wu, *J. Mater. Chem. A* **2018**, *6*, 16439.
[63] D. B. Deutz, N. T. Mascarenhas, J. B. J. Schelen, D. M. de Leeuw, S. van der Zwaag, P. Groen, *Adv. Funct. Mater.* **2017**, *27*, 1700728.
[64] X. Gao, M. Zheng, X. Yan, J. Fu, M. Zhu, Y. Hou, *J. Mater. Chem. C* **2019**, *7*, 961.
[65] R. Senthilkumar, K. Sridevi, J. Venkatesan, V. Annamalai, M. S. Vijaya, *Ferroelectrics* **2005**, *325*, 121.
[66] K. L. Ng, H. L. W. Chan, C. L. Choy, *IEEE Trans. Ultrason. Ferroelectr. Freq. Control* **2000**, *47*, 1308.
[67] X. Cai, C. Zhong, S. Zhang, H. Wang, *J. Mater. Sci. Lett.* **1997**, *16*, 253.
[68] X. F. Liu, H. J. Sun, C. X. Xiong, C. Y. Zhang, H. Zheng, M. Wei, *IEEE Int. Symp. Appl. Ferroelectr.* **2009**, 1.
[69] K. Han, A. Safari, R. E. Riman, *J. Am. Ceram. Soc.* **1991**, *74*, 1699.
[70] D. K. Das-Gupta, *Proc. - Int. Symp. Electrets* **1996**, 807.